

Probing Stellar Populations and Interstellar Medium in Early-Type Central Galaxies

Vanessa Lorenzoni,^{1*} Sandro B. Rembold,¹ Reinaldo R. de Carvalho²

¹*Departamento de Física, CCNE, Universidade Federal de Santa Maria, 97105-900, Santa Maria, RS, Brazil*

²*NAT - Universidade Cidade de São Paulo, 01506-000, São Paulo, SP, Brazil*

6 November 2023

ABSTRACT

In this study, we analyse the characteristics of stellar populations and the interstellar medium (ISM) in 15,107 early-type central galaxies from the SPIDER survey. Using optical spectra from the Sloan Digital Sky Survey (SDSS), we investigate stellar age (Age), metallicity (Z), visual extinction (A_V), and $H\alpha$ equivalent width ($EW_{H\alpha}$) to understand the evolution of the baryonic content in these galaxies. Our analysis explores the relationship between these properties and central velocity dispersion (σ) and halo mass (M_{halo}) for isolated centrals (ICs) and group centrals (GCs). Our results confirm that both ICs and GCs' stellar populations and gas properties are mainly influenced by σ , with M_{halo} playing a secondary role. Higher σ values correspond to older, more metal-rich stellar populations in both ICs and GCs. Moreover, fixed σ values we observe younger Ages at higher values of M_{halo} , a consistent trend in both ICs and GCs. Furthermore, we investigate the ionisation source of the warm gas and propose a scenario where the properties of ionised gas are shaped by a combination of cooling within the intra-cluster medium (ICM) and feedback from Active Galactic Nuclei (AGN) assuming a Bondi accretion regime. We observe inherent differences between ICs and GCs, suggesting that the ratio between AGN kinetic power and ICM thermal energy influences $EW_{H\alpha}$ in ICs. Meanwhile, gas deposition in GCs appears to involve a more complex interplay beyond a singular AGN-ICM interaction.

Key words: galaxies: elliptical and lenticular, cD – galaxies: evolution – galaxies: stellar content – galaxies: star formation

1 INTRODUCTION

In thermalised clusters, a central galaxy, typically bright and massive, resides at the cluster's core. Even in dynamically unrelaxed clusters, the central galaxy can be identified as the one hosting the most massive dark matter sub-halo (Yang et al. 2011). These central galaxies often display a spheroidal morphology and consist of old, metal-rich stars with little to no ongoing star formation (Loubser et al. 2009). They are commonly referred to as Brightest Cluster Galaxies (BCGs) and exhibit distinct physical properties compared to non-central early-type galaxies (ETGs) of similar mass. In fact, they can be up to ten times more luminous than typical ETGs and do not follow the luminosity function observed in other cluster members (Katayama et al. 2003; Dressler 1979a). Moreover, central galaxies residing in massive clusters tend to be associated with radio emission (Von Der Linden et al. 2007; Stott et al. 2012) and possess a cD morphological type (Dressler 1979b; Zhao et al. 2015a,b). Consequently, it is reasonable to consider alternative formation pathways for these objects.

Environmental factors seem to contribute to the evolution of central galaxies. It has been observed (Lacerna et al. 2014) that groups and clusters centrals exhibit distinct characteristics from isolated centrals (halos lacking satellites galaxies). Specifically, centrals in groups or clusters tend to display a redder colour, higher mass, and reduced star formation activity. Moreover, isolated centrals at a fixed

σ have older ages, higher $[\alpha/\text{Fe}]$ ratios, and lower internal reddening compared to their counterparts in groups (La Barbera et al. 2014). These authors also propose that stars in central galaxies of more massive halos are younger, implying that group or cluster centrals formed their stellar components over longer timescales than isolated ones. In a separate investigation, Zhao et al. (2015c) reveal that more massive BCGs predominantly reside in denser regions and more massive clusters when compared to lower mass BCGs.

The formation and evolution of central galaxies remains a complex and unresolved topic, involving internal processes like gas-to-star transformation and feedback from supernovae and AGN, as well as external processes associated with the cluster environment. An example of an environmentally-driven evolutionary process is the cooling flow observed in cool-core clusters. For instance, the ICM gas rapidly (within 10 to 100 million years) loses pressure support and thermal energy through X-ray emission (Gaspari et al. 2013a), namely the cooling flow supplies cold gas to the central galaxy, which may induce star formation. McNamara et al. (1996) present clear evidence of this process as blue and ultraviolet excesses indicate star formation in the vicinity to the central galaxy. Cold molecular gas associated with the cooling flow and $H\alpha$ -emitting filaments from young stars near the cluster core have also been observed (Edge 2001; Salomé & Combes 2004; Revaz et al. 2008; Salomé et al. 2006). Moreover, McDonald et al. (2012) investigate a galaxy cluster at redshift $z = 0.596$ with an exceptionally strong cooling flow and observe a massive starburst in the central galaxy. However, it is noteworthy that the cooling flow rates often fall below predictions from the classic model (McNamara & O'Connell 1989), which suggests an intense star formation rate

* E-mail: vanessa.lorenzoni@acad.ufsm.br

of $1,000 M_{\odot} \text{ yr}^{-1}$ (Fabian 1994). Observations indicate that centrals exhibit star formation rates ranging from approximately 1% to 10% of the predicted value (Edge 2001; O’Dea et al. 2008; McDonald et al. 2010, 2011), implying that the ICM is reheated by an external source (Fabian 1994).

Observational and simulation-based studies, such as Croton et al. (2006); McNamara & Nulsen (2007) and Birzan et al. (2008), suggest that radio-mode feedback acts as a regulator of gas supply in cooling flows. The feedback mechanism produces powerful jet structures with radio-emitting lobes, observable as X-ray cavities causing depressions in surface brightness. The spatial correspondence between these structures and the radio jets are important signatures of the interplay between AGN feedback and the host environment (Birzan et al. 2004; Croston et al. 2011; Hlavacek-Larrondo et al. 2015). However, the mode and efficiency of the accretion mechanism responsible for producing radio jets as well as the energy required to regulate cooling flows are still debated. Best et al. (2006); Allen et al. (2006); Hardcastle et al. (2007); Fujita et al. (2014) argue that jet formation is primarily driven by accretion of hot gas from the X-ray emitting medium, known as Bondi accretion (Bondi 1952). On the other hand, Voit & Donahue (2015) propose a model of precipitation-regulated AGN feedback in central galaxies, where gas from the ICM flows toward the cluster centre, fuelling the supermassive black hole (SMBH) through cold and chaotic accretion (Gaspari et al. 2013b). This scenario of jet formation via cold gas accretion is also supported by McNamara et al. (2011). In both scenarios, the jets produced expel gas from the galaxy, leading to self-regulation between AGN feedback and the feeding of the SMBH. AGN feedback can not only regulate the cooling flow in cool-core clusters but it also impacts the properties of the central galaxy’s baryonic content: it is crucial for reproducing the bright end of the galaxy luminosity function and explaining the red colours and chemical composition of central galaxies, indicating a short duration of the star formation epoch (Springel et al. 2005).

Interactions between galaxies within clusters are also frequently observed, with dynamic friction (Chandrasekhar 1943) playing a crucial role in the migration of massive galaxies towards the centre of galaxy clusters. This process drives the merging and growth of central galaxies, while also triggering star formation and black hole activity. Consequently, it provides a potential explanation for the observed high masses and the very extended radial surface brightness distributions found in cD galaxies (Oemler 1976). Oyarzún et al. (2022) suggest that mergers in central galaxies can trigger rapid and intense star formation episodes, leading to stellar mass growth. Central galaxies with higher galaxy total mass exhibit older stellar populations and appear to have formed over shorter time-scales than those with lower stellar mass. Somboonpanyakul et al. (2022) and La Barbera et al. (2014) propose mergers with gas-rich galaxies as the primary fuel source for AGNs in high-redshift BCGs. Moreover, mergers with gas-rich galaxies potentially explain the higher metallicity and younger ages observed in group centrals compared to isolated centrals.

The assembly history of central galaxies varies with central galaxy mass and host halo, as indicated by previous studies (La Barbera et al. 2014; Oyarzún et al. 2022). Despite progress in understanding their formation and evolution, several questions remain unanswered. Specifically, the development of the stellar and gas content of central galaxies and the relative contributions of internal and external processes in the assembly history of such objects are still open questions. In this study, we address these questions by investigating the stellar population properties of central galaxies as a function of their σ (a proxy for total galaxy mass) and M_{halo} (a proxy for the environ-

ment). We conduct a comprehensive analysis of stellar populations and ionised gas properties in a sample of central galaxies spanning various ranges of σ and M_{halo} . We quantitatively investigate the dependencies of these parameters in both regimes, employing simple analytical functions for parameterisation. Furthermore, we examine the observed characteristics of ionised gas within a scenario that considers the interplay between feedback from the central galaxy’s nuclear activity and intracluster gas cooling, assuming the Bondi accretion model, to regulate the gas accretion into the central galaxy.

The paper is structured as follows: Section 2 provides details on the central galaxy sample selection, the stacking procedure and how we run the stellar population synthesis; In Section 3, we present our results, considering isolated and group centrals separately. In Section 4 we discuss the main findings of our investigation presenting a model of the gas content in central galaxies. Finally, our conclusions are summarised in Section 5. Throughout the present work, we adopt $\Omega_m = 0.3$, $\Omega_{\Lambda} = 0.7$ and $H_0 = 100 h \text{ km s}^{-1} \text{ Mpc}^{-1}$, with $h = 0.7$.

2 DATA AND METHODS

Our sample is based on Spheroid’s Panchromatic Investigation in Different Environmental Regions – SPIDER I (La Barbera et al. 2010), which includes 39,993 ETGs within the redshift range $0.05 < z < 0.095$ from the Sloan Digital Sky Survey Data Release 6 (Adelman-McCarthy et al. 2008, SDSS-DR6). We apply an absolute r-band Petrosian magnitude limit of $M_r < -20$, corresponding to the separation between *bright* and *ordinary* elliptical galaxies (Capaccioli et al. 1992; Graham & Guzmán 2003), which aligns approximately with the upper redshift limit of $z = 0.095$, where SDSS spectroscopy is complete. The lower redshift limit avoids the aperture effect in our measurements.

For selecting ETGs, we adopt the criteria established by La Barbera et al. (2010). We set the SDSS attribute *fracDev_r* > 0.8 to select bulge-dominated systems and the attribute *eClass* < 0 to determine spectral type based on principal component analysis decomposition. We also include only objects with $\sigma > 100 \text{ km s}^{-1}$, to remove the low-mass ETGs. We exclude galaxies with low internal extinction ($E(B - V) < 0.1 \text{ mag}$) to remove contamination by lenticular galaxies, as well as spectra with signal-to-noise ratio (S/N, per Å) in the H_{β} region smaller than 14, 27, and 21 for $\sigma = 100, 200$, and 300 km s^{-1} respectively; such S/N cuts correspond to the lowest S/N quartile in the given σ bin. We also verify the morphological classification of these galaxies using the Galaxy Zoo project (Lintott et al. 2011). However, given that not all galaxies have Galaxy Zoo classifications, we apply additional selection criteria based on the quality of the two-dimensional Sérsic fits to the surface brightness distribution, as described in La Barbera et al. (2014). In the end, we are left with 20,977 ETGs with optical spectra, σ and its uncertainty (σ_{err}) extracted from SDSS-DR12 (Alam et al. 2015). The uncertainties in σ are typically less than 10 km s^{-1} , except for 95 central galaxies (with the maximum σ_{err} value being 13.68), a negligible figure considering all central galaxies in our sample.

2.1 Characterisation of the galaxy host environment

The galaxy host environment is characterised by the Yang Catalogue (Yang et al. 2007, hereafter Y07). Y07 is constructed using a halo mass finder algorithm applied to the New York University Value-Added Galaxy Catalogue (Blanton et al. 2005, NYU-VAGC). Galaxies within a common dark matter (DM) halo form a group and

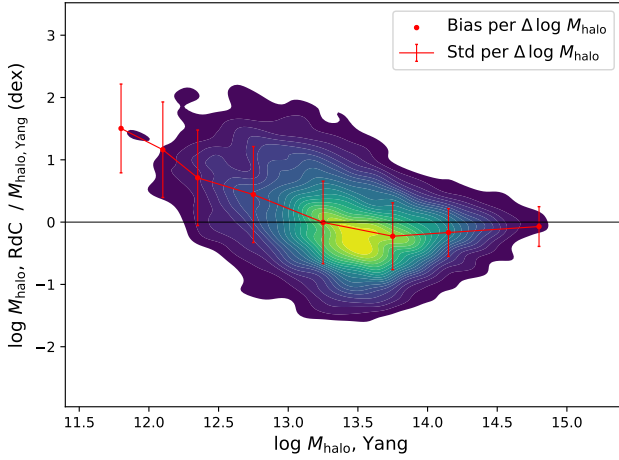


Figure 1. Comparison between the halo mass measurements obtained by de Carvalho et al. (2017) and by Yang et al. (2007). The red dots and lines indicate the bias and standard deviation for specific halo mass ranges, respectively.

are classified as either satellite or central galaxies, based on their stellar mass.

Central galaxies are identified as the most massive galaxy within the DM halo and can be distinguished in two categories: 1) isolated centrals (IC), those occupying a single DM halo and no other galaxy; 2) group centrals (GC), those sharing a DM halo with other satellite galaxies. Distinct evolutionary processes may shape the physical properties of ICs and GCs differently. Therefore, we investigate these two populations separately. Y07 determine the DM halo mass by the total stellar mass of the group, which must satisfy the condition $M_{\text{halo}} \geq 10^{12} h^{-1} M_{\odot}$. Our sample includes 15, 107 early-type central galaxies, where 10, 575 are ICs and 4, 532 are GCs.

We compare halo masses obtained using the shift-gapper technique by de Carvalho et al. (2017) with those estimated by Yang et al. (2007) to evaluate systematic errors in M_{halo} measurements. The comparison, shown in Figure 1, is based on the dispersion and bias generated by these two methods for specific ranges of the Yang halo mass ($\Delta \log M_{\text{halo}}$).

2.2 Stacking galaxy spectra by their σ and M_{halo}

To enhance the S/N of optical spectra, we perform spectral stacking by median-combining the flux-normalised individual spectra within bins of σ and M_{halo} . The resulting stacked spectra, corrected for redshift, is computed as the median of the available spectra within each bin. The flux uncertainties, for a given wavelength, are estimated from the standard error of the median across all spectra entering each final stacked spectrum. Thus, our sample is distributed across 71 stacks, with σ ranging from 100 to 323 km s⁻¹ and M_{halo} spanning from $10^{11.6}$ to $10^{15.3} M_{\odot}$. The bin size is set to vary in steps of 10 km s⁻¹ for σ , except for the highest-value bins. For M_{halo} , we vary the bin width in steps of 0.25, 0.40, 0.50, and 1.00 dex. The initial range for M_{halo} begins at $10^{11.6} M_{\odot}$, as our sample does not include any halos below this threshold. Finally, we exclude from further analysis all stacks containing less than 5 galaxies, thus ensuring a minimum representative number of objects per stack. The number of galaxies and the S/N per bin are summarised in Tables A1, A2 and A3. The ICs, which predominantly occupy halos with masses below $10^{13.5} M_{\odot}$, are concentrated in 54 bins. In contrast, GCs are predominantly associated with higher M_{halo} values, and yield 61 bins of GC galaxies.

This highlights the connection between galaxy properties and DM halos, as reflected in the stellar-to-halo mass relation (SHMR), where more massive galaxies are typically found in more massive halos. It is important to note that the stacking process enhances the spectral S/N, but removes individual signatures from each galaxy, providing a representative spectrum of the entire population.

2.3 Stellar population properties: Spectral synthesis analysis using STARLIGHT code

To estimate Age, Z and A_V , we use the spectral synthesis method by employing the STARLIGHT software (Cid Fernandes et al. 2005), which performs spectral synthesis by comparing the observed galaxy spectrum with a set of simple stellar population (SSP) models, searching for the combination of SSPs that best represents the observed spectrum. In this study, we use a set of 108 solar-scaled SSPs models from the Medium resolution INT Library of Empirical Spectra (MILES) galaxy spectral library (Vazdekis et al. 2010). These models are constructed using the Kroupa universal Initial Mass Function (IMF) and cover ages ranging from 0.5 to 17.78 Gyr, with $Z = 0.004, 0.008, 0.019$ and 0.03 . The possible occurrence of non-solar abundance ratios in our sample of galaxies is not expected to affect significantly the derived stellar population parameters, as discussed in La Barbera et al. (2014).

The MILES models have a spectral resolution of approximately 2.5 Å and cover a wavelength range from 3, 525 to 7, 500 Å. In line with the study by La Barbera et al. (2014), we conduct the synthesis using the wavelength range from 4, 000 to 5, 700 Å, with 5, 200 Å as the normalisation wavelength; the exclusion of the spectral range above 5, 700 Å is motivated by the presence of particularly IMF-sensitive absorption features (like Na and TiO) in this region. We apply the Cardelli et al. (1989) extinction law (suitable for systems with low levels of star formation) and mask the main SDSS optical emission lines. We estimate the light-weighted Age and Z following Cid Fernandes et al. (2005, , their Equations 2 and 5), while the A_V parameter is directly provided by the STARLIGHT output.

To ensure the robustness of our results, we perform additional syntheses using an alternative set of SSPs, the Granada-MILES (GM) models (Cid Fernandes et al. 2013). GM templates are a combination of Granada models from González Delgado et al. (2005) (for ages younger than 63 Myr) and MILES models. The construction of the SSPs uses a Salpeter IMF and includes the evolutionary tracks by Girardi et al. (2000), with the exception of ages ≤ 3 Myr, where the Geneva evolutionary tracks are employed (Schaller et al. 1992; Schaerer et al. 1993a,b; Charbonnel et al. 1993) and a spectral resolution of approximately 2.3 Å. We convolve the GM SSPs spectra to coincide the spectral resolution of the MILES models and also select only the templates with the same age and Z , enabling a direct comparison between them. We have found (Figure A1) that differences in SSPs can indeed affect the derived stellar population parameters; however, the derived EWH α values are entirely insensitive to the chosen SSPs, and all stellar population parameter trends with σ and M_{halo} are consistent. We are therefore confident that the observed σ and M_{halo} trends that are presented and discussed in Sect. 3 are not dependent on the choice of SSPs models.

To estimate the equivalent width of H α (EWH α), we extend the synthesis solution obtained previously up to 7, 000 Å to include H α emission. We then subtract the synthetic and observed spectra to obtain the residuals, which contain only the contribution of emission lines. Finally, the H α flux (Gaussian area) is divided by the mean level of the stellar continuum at the line position, obtained from the synthetic spectrum. The only purpose of this second synthesis run up

to 7,000 Å is to allow for a straightforward measurement of EWH α ; the stellar population parameters that will be presented and discussed in the remainder of the paper are those obtained with the synthesis limited to 5,700 Å.

Uncertainties in the studied properties are estimated using the bootstrap method. In short, we perform a random selection of a single object among all galaxies in a given stack; this operation is repeated N times, where N is the total number of galaxies in the respective stack. In this process, not all galaxies of the stack are selected, because a given galaxy can be selected multiple times. Subsequently, the entire stack creation process is performed with the newly selected galaxies. Then, we conduct the stellar population synthesis and estimate each property mentioned before. This procedure is repeated 1,000 times for each stack. To obtain the uncertainty in the parameters, we calculate the standard deviation for each stack and property.

3 RESULTS

3.1 Exploring the trends in stellar population and interstellar medium properties

In Figure 2, we provide an illustrative overview of all parameters, emphasising their inherent dependencies on both σ and M_{halo} , despite the presence of significant scatter. To further explore these dependencies, we narrow our focus to specific M_{halo} ranges. As shown in Figure 3, we examine the behaviour of each observable as a function of σ for both ICs and GCs, employing three distinct M_{halo} bins, distinguished by different colours, to simplify the visualisation of systematic trends. These M_{halo} ranges were chosen for their availability to both ICs and GCs. Also, we have included the curves obtained for ICs as dotted lines in the GCs panels, making a direct comparison easier.

3.1.1 Stellar Age - Age

As far as ICs are concerned, we see that Age increases up to approximately $\sigma \sim 200 \text{ km s}^{-1}$ and then reaches a plateau (panel b of Figure 3). Higher values of M_{halo} are associated with older stellar populations at a given σ . However, for σ values lower than 150 km s^{-1} , the large uncertainties make it more difficult to interpret the trend. Notably, there is an age difference of approximately 2 Gyr between the low and high M_{halo} bins at a given σ . These trends are basically the same as those exhibited by GCs (panel c of Figure 3), although with a greater scatter due to the lower number of galaxies per bin. It is worth noticing that there are no GCs with $\sigma \geq 200 \text{ km s}^{-1}$ in $12.0 \leq \log M_{\text{halo}} \leq 12.25$. Despite these findings being consistent with those presented by La Barbera et al. (2014), we do not observe any discernible difference between ICs and GCs, contrary to their discussion. This crucial distinction will be further addressed in Sect. 4.1.

3.1.2 Stellar Metallicity - Z

We note a tendency for the stellar population to be more metal-rich as σ increases, the so called mass-metallicity relation; this holds for ICs and GCs indistinctly (panels e and f of Figure 3). We do not find any dependence on M_{halo} , as indicated by the overlapping curves, except for centrals with $\sigma \lesssim 150 \text{ km s}^{-1}$, for which we note a slight increase in Z for the intermediate M_{halo} bin. This result is in agreement with those reported by La Barbera et al. (2014). There seems to be no

difference between ICs and GCs as far as the behaviour of Z with σ is concerned, albeit with greater scatter for GCs.

3.1.3 Visual Extinction - A_V

Examining panels h and i of Figure 3 we identify a decrease in A_V as σ increases, for ICs and GCs. Particular, for ICs we find a systematic increase in A_V as we probe centrals with $\sigma \lesssim 200 \text{ km s}^{-1}$ and greater M_{halo} . For $\sigma \geq 200 \text{ km s}^{-1}$ the curves overlap and A_V becomes insensitive to M_{halo} . Conversely, there appears to be no correlation between A_V and M_{halo} for GCs. Nevertheless, the scatter is significantly large, making it inconclusive to assert that the same systematic difference with M_{halo} observed in ICs is also present in GCs.

3.1.4 Equivalent width of H α - EWH α

In line with A_V , ICs exhibit a decreasing trend in EWH α as σ increases. Notably, we observe a systematic variation with M_{halo} , with centrals with higher EWH α inhabiting more massive halos. The difference in EWH α amounts to approximately 0.6 Å, which is significantly larger than the errors in EWH α for the two lowest M_{halo} bins in the plot. The relationship between EWH α and σ is less pronounced for GCs. Moreover, no apparent correlation between EWH α and M_{halo} is observed for GCs. The similarity in the results for A_V and EWH α holds true for both ICs and GCs, and further details will be discussed in Sect. 4.3.

3.2 Correlating central galaxies properties with σ and M_{halo}

In the previous section, we provided a qualitative description of the studied properties, Age, Z , A_V and EWH α , as a function of σ and M_{halo} , revealing a dependence on these parameters (Figures 2 and 3). Consequently, we conduct a quantitative analysis of these dependencies assuming a linear combination of σ and M_{halo} to represent the parameters describing the stellar and gas content:

$$Y \sim \sigma^A M_{\text{halo}}^B, \quad (1)$$

where A and B are free parameters and Y represents the quantity under study.

The choice of a power law is motivated only by its simplicity. Hence, we conduct a least squares fit to the function $\log Y = A \log \sigma + B \log M_{\text{halo}} + C$, with uncertainties in Y given by standard deviation, estimated via bootstrap (Sect. 2.3).

To incorporate uncertainties in σ and M_{halo} , we employ the bootstrap method, performing 1,000 fits. The σ uncertainty (σ_{unc}) for each bin is determined through error propagation on the mean σ values, considering the 95th percentile of σ_{err} . For each bin and fit iteration, we generate a new σ value from a standard normal distribution centred around the mean value of the σ range, with an uncertainty of σ_{unc} .

In the case of M_{halo} , to prevent overlap resulting from the narrow gap between M_{halo} ranges, we assign a random value between zero and 1.5 (the maximum absolute bias between the two methods, obtained from Fig. 1), to each M_{halo} measurement, allowing for positive and negative variations. In each fit iteration, we calculate the new M_{halo} by multiplying the random value by the corresponding bias for each M_{halo} range and adding it to the mean value of M_{halo} in the bin. This approach ensures a consistent directional shift across all M_{halo} ranges. Furthermore, we consider random errors by applying

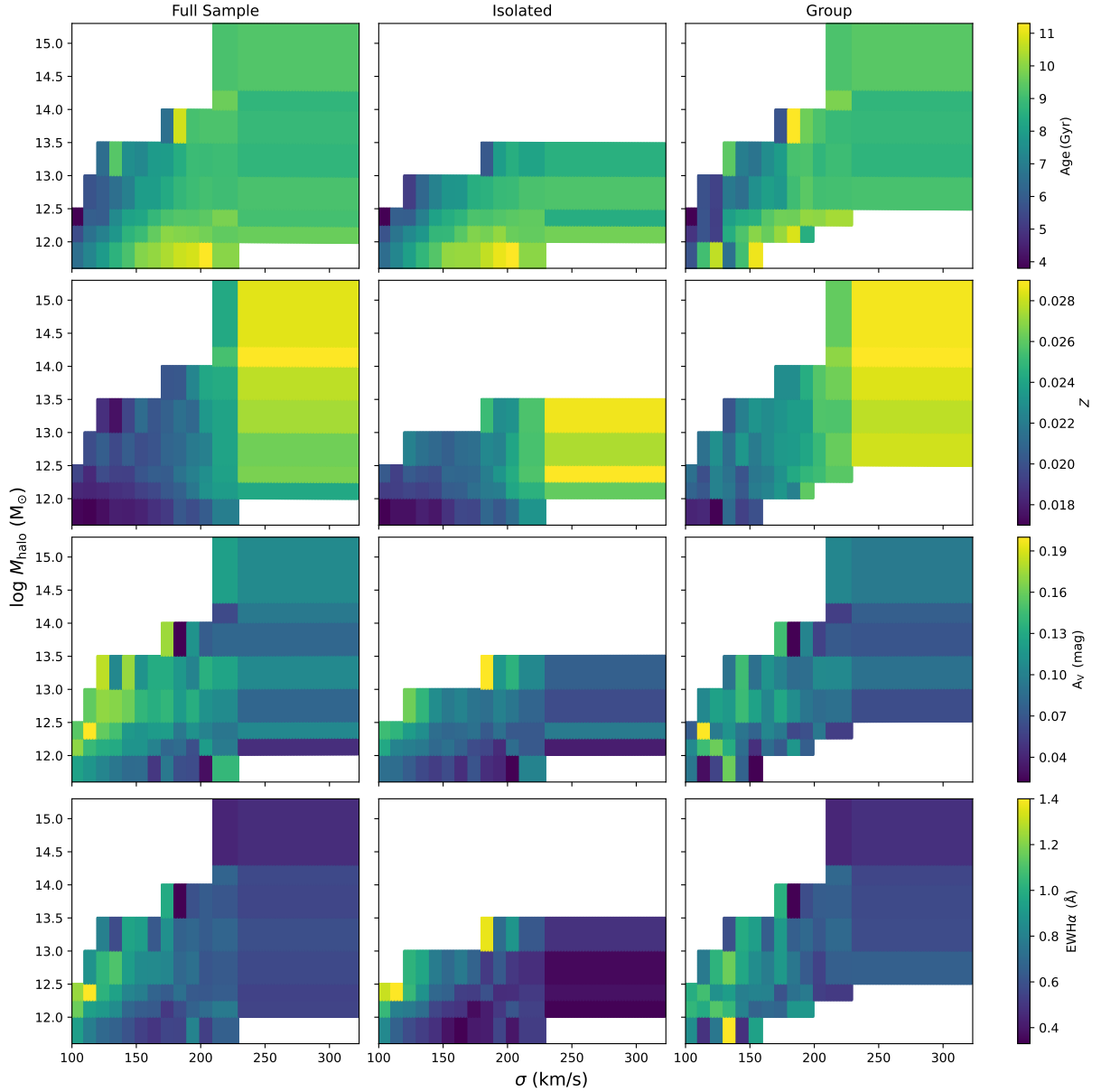


Figure 2. Variations in Age, Z , A_V , and $\text{EWH}\alpha$ as a function of σ (horizontal axis) and M_{halo} (vertical axis) are shown from the top to bottom, respectively. The full sample, as well as ICs and GCs, are illustrated from left to right, respectively. The physical properties are represented by colours.

a random distribution with galaxy-to-galaxy σ_{err} to the new M_{halo} value.

The best-fit A and B coefficients were obtained by computing the weighted average of the coefficients obtained from the 1,000 bootstraps. The uncertainties are estimated by determining the standard deviation of the 1,000 coefficients, weighted according to their respective errors.

Regarding the Age parameter specifically, we have observed that the best-fit coefficients grossly overestimate the ages of central galaxies at low σ values. This is due to a large spread in the mean stellar age across the different bootstrap realisations, possibly related to a larger variety in stellar ages of the galaxies in such stacks. At high σ , we observe a much lower spread in Age, suggesting that galaxies at this σ range are less varied regarding this parameter. Using the spread in Age as an estimate of its uncertainty results in an unsatisfactory parameterisation, since older central galaxy bins, characterised by

lower spreads, influence disproportionately the solution, causing it to perform poorly for younger ages. Consequently, in order to find coefficients that describe as accurately as possible the overall trends of all stacks, we ignore the Age uncertainties in the fits.

The values of the coefficients A , B and C , along with their corresponding uncertainties, are shown in Table 1 and confirm the trends observed in Figure 3. The coefficient C will no longer be considered, as it works only as a normalisation parameter. For instance, when examining the coefficients A for Age, it becomes apparent that GCs exhibit a weaker correlation with σ compared to ICs. In terms of the relationship with M_{halo} , ICs demonstrate a value approximately twice as high as GCs. On the other hand, GCs display a stronger correlation between Z and σ compared to ICs. Conversely, the association between Z and M_{halo} is less pronounced for GCs. It is noteworthy that the coefficients B are small, indicating a weak dependence of Z on M_{halo} . The correlation coefficients between A_V and σ are com-

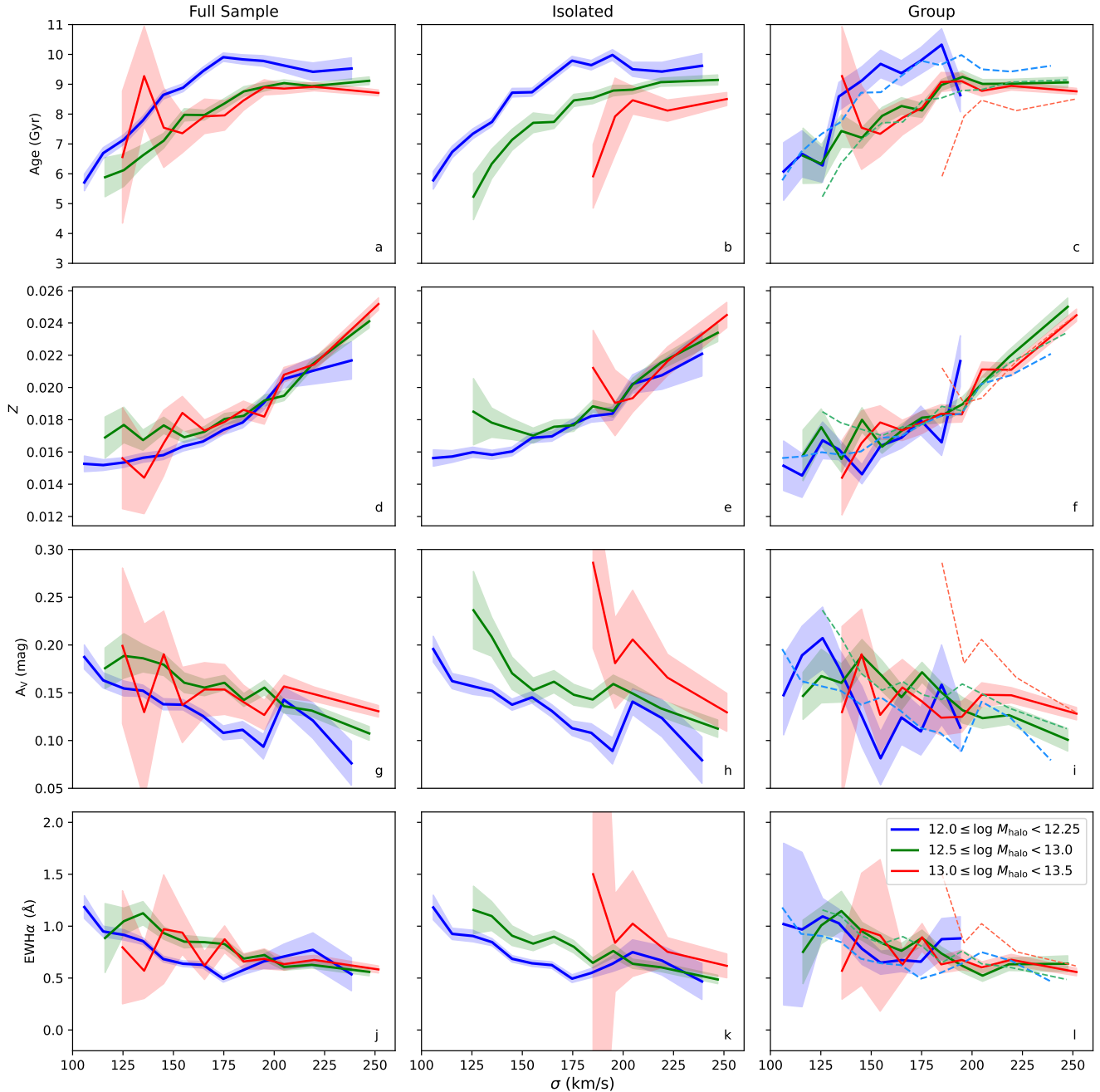


Figure 3. Relationship between Age, Z , A_V , and $\text{EWH}\alpha$ with σ , depicted from top to bottom, respectively. The full sample, along with ICs and GCs, is presented from left to right, respectively. Additionally, we included three M_{halo} ranges, distinguished by colours.

parable for ICs and GCs, considering the uncertainties. However, when examining the correlation between A_V and M_{halo} , ICs show a significantly stronger relation compared to GCs, where the correlation is very weak. Regarding the correlation between $\text{EWH}\alpha$ and σ , ICs and GCs display a similar level of correlation, although slightly weaker for GCs. On the other hand, the correlation coefficients between $\text{EWH}\alpha$ and M_{halo} are significantly smaller for GCs, being approximately ten times smaller than those for ICs. It is important to note that the correlation patterns between A_V and $\text{EWH}\alpha$ observed in Sect. 3.1 are also evident in the coefficients A and B , considering the uncertainties, for both ICs and GCs. Therefore, we highlight that the

correlation between all properties, regardless of the sample, shows a stronger association with σ than with M_{halo} .

To assess the quality of the parameterisation, we present Figure 4, where we plot the observed properties against the predicted values obtained from Eq. 1 using the best-fit coefficients from Table 1. The panels of Figure 4 follow the same arrangement as Figure 3, presenting Age, Z , A_V , and $\text{EWH}\alpha$ from top to bottom, respectively. From left to right, the panels display the results for the full sample, ICs, and GCs. The dots represent the physical properties values, with their corresponding M_{halo} indicated by colours. Vertical error bars are included to represent the standard deviation calculated

using the bootstrap process described in Sect. 2.3. We provide the Pearson coefficient (r) as a measure of the correlation between the observed and predicted values. Upon examining the panels b and c, a curved relationship is noticed, particularly for ICs, where the predicted values tend to overestimate the Age for $\log \text{Age} < 0.8$. This non-linearity suggests that the functional form presented in Eq. 1 may be inadequate to fully describe the relationship between Age, σ , and M_{halo} . While this curvature consistently appears for central galaxies across different M_{halo} , the primary source of discrepancy between the observed and predicted values is attributed to σ . It seems that the Age follows a relation with σ that is less steep than a simple power law. Nevertheless, considering the relatively high Pearson coefficients ($r = 0.798, 0.872, \text{ and } 0.708$ for the full sample, ICs, and GCs, respectively), these parameterisations capture most of the physical links between Age, σ , and M_{halo} . However, it is important to interpret these coefficients with caution. The parameterisation for Z demonstrates exceptional performance across all sub-samples. The scatter plot comparing the observed and predicted values of Z closely follows a 1:1 relation, as evidenced by the high Pearson coefficients ($r = 0.909, 0.895, 0.902$ for the full sample, ICs, and GCs, respectively). Although Eq. 1 effectively captures the relationship between Z and both σ and M_{halo} , it is important to note that this is primarily due to the well known Mass-Metallicity relation and that M_{halo} contributes a small fraction to the final correlation. For A_V , we achieve a good agreement between the observed and predicted values in ICs. Pearson’s coefficient remains significant, with a value of $r = 0.822$ (panel h). However, the low Pearson coefficient of 0.287 for GCs (panel i) indicates a predominance of dispersion in the data points, revealing a limitation in our parameterisation to accurately describe the relationship between A_V , σ and M_{halo} . Similarly, for $\text{EWH}\alpha$, we also find a satisfactory agreement between the observed and predicted values for ICs, as indicated by the higher Pearson coefficient of $r = 0.839$ (panel k). However, for GCs, the scatter becomes more pronounced, resulting in a Pearson coefficient of 0.572 (panel l). Despite the differences between the predicted and observed values being influenced by scattering for GCs, we consider the parameterisation to be a reasonable description for both A_V and $\text{EWH}\alpha$.

In a nutshell, the main findings of the parameterisation presented in Table 1 emphasise that the parameter σ plays a more significant role in describing the observed properties of central galaxies compared to M_{halo} . The influence of M_{halo} is generally small, especially for GCs. Also, ICs exhibit stronger correlations between most parameters and both σ and M_{halo} . However, there is an exception in the case of the correlation between Z and σ , which is stronger for GCs. Therefore, predicting the behaviour of these quantities with respect to σ and M_{halo} is more straightforward for ICs than for GCs. The implications of these findings will be discussed in the upcoming section.

4 DISCUSSION

Understanding the evolution of central galaxies is a complex task, as it is influenced by many factors. The mass of the halos they inhabit plays a crucial role in determining their evolutionary trajectory. Also, σ is a vital parameter when studying their stellar population and ionised gas content. A study conducted by La Barbera et al. (2014) focused on early-type central galaxies find that as σ increases, these systems tend to be older. Furthermore, within a given σ range, central galaxies in more massive halos appear to be younger. Adding to the intricacy of the situation is the interaction between the thermal energy of the intracluster medium and the kinetic power of the AGN, which introduces significant complexity to an already unresolved problem.

4.1 The Impact of the Environment on the Star Formation History of Central Galaxies

When studying how the environment influences galaxy properties, it is important to define the concept of “environment” carefully. La Barbera et al. (2014) use M_{halo} as an indicator of environment and consider a central galaxy as isolated when the $\log M_{\text{halo}} \leq 12.5$. However, using Yang’s classification of each structure, we observe contamination between ICs and GCs when employing La Barbera’s definition of an IC. Specifically, there are 2011 ICs ($\sim 15\%$) with $\log M_{\text{halo}} \geq 12.5$ and 889 GCs ($\sim 24\%$) with $\log M_{\text{halo}} \leq 12.5$. In this study, we utilise Yang’s structure classification to explore potential differences in the stellar populations of ICs and GCs. La Barbera et al. (2014) suggest that the difference between ICs and GCs stems mainly from ICs being defined as centrals with $\log M_{\text{halo}} \leq 12.5$. However, considering the contamination mentioned earlier, this assertion appears questionable. The trend with σ and M_{halo} is consistent for both ICs and GCs. This implies that regardless of whether the central galaxy is replenished with gas from its own halo (in the case of ICs) or from gas-rich systems that have been accreted (in the case of GCs), the final star formation history (SFH) remains the same. It is crucial to remember that such a trend between Age and σ is observed for galaxies in general (e.g., González Delgado et al. (2015)). Regarding the Z, panels e and f of Figure 3 yield results consistent with La Barbera et al. (2014). Specifically, we find that Z increases with σ , following the Mass-Metallicity relation initially established by Lequeux et al. (1979). Furthermore, in agreement with La Barbera et al. (2014), we do not observe any dependence on M_{halo} , except for a small difference between ICs and GCs when $\sigma \leq 135 \text{ km s}^{-1}$, with ICs being slightly more metal-rich than their counterparts in GCs.

The relationship between Age, Z, and M_{halo} has been a topic of debate in the literature. In a study by Oyarzún et al. (2022) focusing on passive central galaxies from the MaNGA survey (Bundy et al. 2015), it is observed that central galaxies are older and more metal-poor in more massive halos. The discrepancy between their findings and ours could be attributed to their selection of passive galaxies based on their spatially integrated specific star formation rate, regardless of their morphological type. In contrast, Scholz-Díaz et al. (2022) find that, at a fixed σ , central galaxies tend to be more metal-poor in more massive halos. This difference may arise because our sample of central galaxies consists exclusively of ETGs, while the authors include both early- and late-type galaxies in their analysis.

The age of a galaxy reflects its entire SFH, but the numerical values alone cannot distinguish between a continuous, extended SFH and an old population followed by a quiescent phase with a recent burst. To address this issue, we present Figure 5, which shows the cumulative SFH for each bin of σ (indicated by the horizontal arrow) and M_{halo} (vertical arrow) in the full sample. Each box represents the percentage of the cumulative mass of each SSP as a function of look-back time (in Gyr). The figure demonstrates that, for a fixed σ , the SFH becomes more extended as M_{halo} increases. Likewise, for a fixed M_{halo} , the SFH is more extended for centrals with lower σ . Consequently, lower values of σ and M_{halo} (lower left part of Figure 5) correspond to more extended SFHs, while the opposite holds true for the upper right part of the figure. In a study by De Lucia et al. (2006), which combines N-body simulations with semi-analytic techniques to investigate the formation and evolution of elliptical galaxies in a hierarchical merger model, they find that lower-mass elliptical galaxies exhibit extended star formation time-scales, consistent with our findings.

The similarity in the variations of Age and Z with σ and M_{halo} for both ICs and GCs indicates that the mechanisms by which centrals retain their hot gas halo (in the case of ICs) and accrete gas from

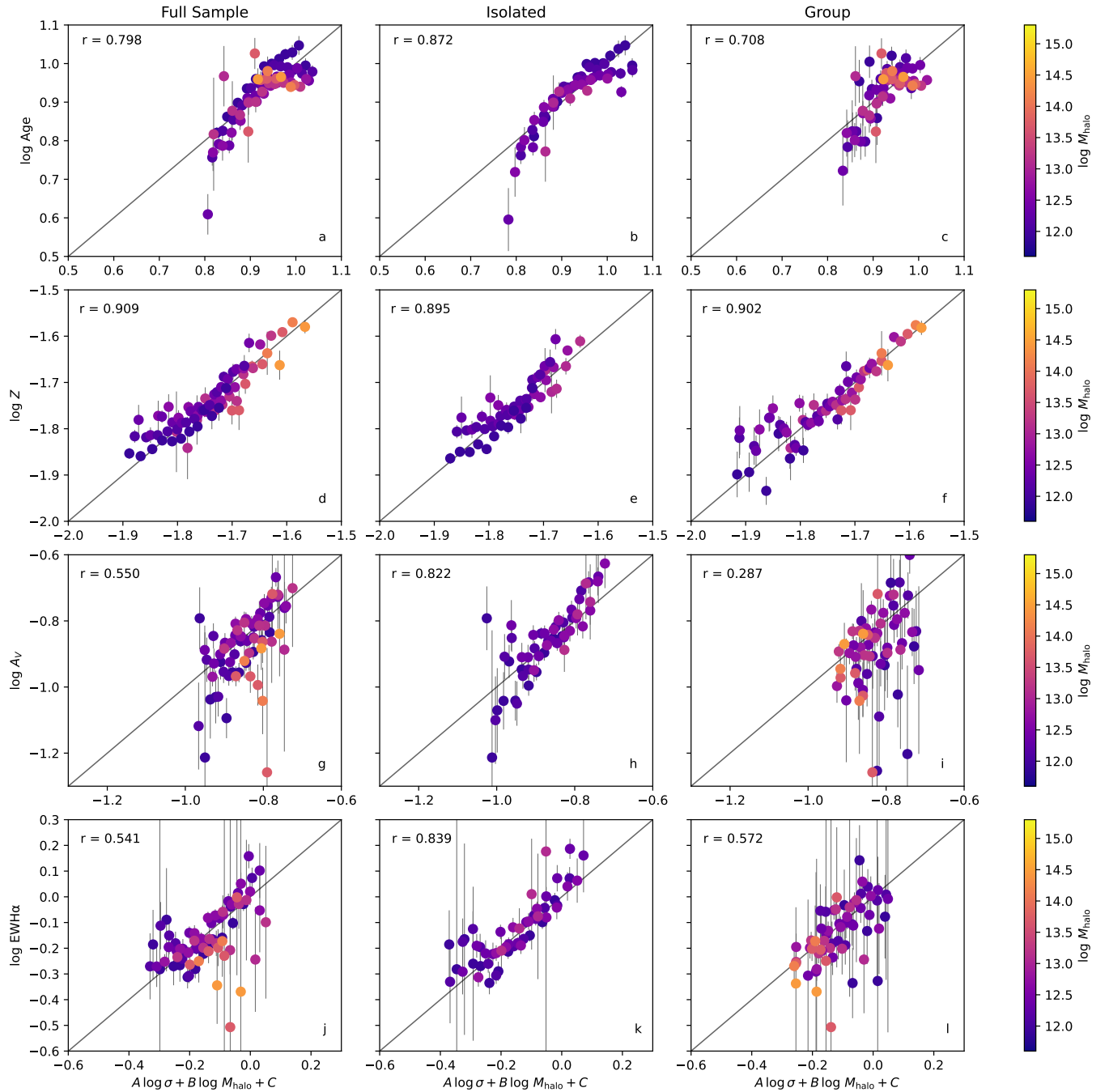


Figure 4. Comparison between observed properties and their corresponding predicted values obtained from Equation 1. The sequence of panels follows same pattern of Figure 2. Central galaxies are represented by dots, with their corresponding M_{halo} ranges indicated by colours. Vertical error bars are derived from the bootstrap process detailed in Sect. 2.3. Additionally, the degree of correlation between the observed and predicted values, estimated by the Pearson coefficient r , is shown in all panels.

the surroundings (in the case of GCs) are not fundamentally different. This implies that as gas cools down and flows into the galaxy, triggering the formation of new stars, there is an increase in Z and a decrease in Age, regardless of whether the gas is retained from the halo or acquired through accretion.

4.2 Probing the origin of the emission lines

In this section, we investigate the ISM properties by analysing A_V and the $EWH\alpha$, which reflect the galaxy's gas content. However, it is important to note that the mechanisms responsible for producing emission lines and interstellar extinction differ. While a galaxy showing the ionisation pattern typical of LINERs may exhibit signatures of $H\alpha$ and other spectral lines generated in the narrow line region near the galaxy nucleus, the effects of extinction can impact any re-

Table 1. Correlation coefficients A , B and C (column 1) obtained from Equation 1, for each sub-sample (column 2), between Age (column 3), Z (column 4), A_V (column 5), and $\text{EWH}\alpha$ (column 6), versus $\log \sigma$ and $\log M_{\text{halo}}$. The errors are quoted at the 1σ level.

Coefficient	Environment	Age	Z	A_V	$\text{EWH}\alpha$
A	Full Sample	0.62 ± 0.03	0.58 ± 0.04	-0.54 ± 0.15	-0.91 ± 0.18
	Isolated	0.70 ± 0.05	0.49 ± 0.04	-0.62 ± 0.12	-1.14 ± 0.15
	Group	0.53 ± 0.05	0.75 ± 0.01	-0.55 ± 0.05	-0.82 ± 0.03
B	Full Sample	-0.033 ± 0.008	0.027 ± 0.008	0.07 ± 0.02	0.09 ± 0.03
	Isolated	-0.08 ± 0.04	0.03 ± 0.02	0.13 ± 0.07	0.16 ± 0.08
	Group	-0.033 ± 0.008	0.012 ± 0.004	0.016 ± 0.011	0.011 ± 0.007
C	Full Sample	-0.035 ± 0.13	-3.35 ± 0.14	-0.34 ± 0.33	0.95 ± 0.45
	Isolated	0.38 ± 0.55	-3.21 ± 0.24	-1.00 ± 0.82	0.56 ± 0.98
	Group	0.15 ± 0.14	-3.59 ± 0.07	0.27 ± 0.09	1.60 ± 0.08

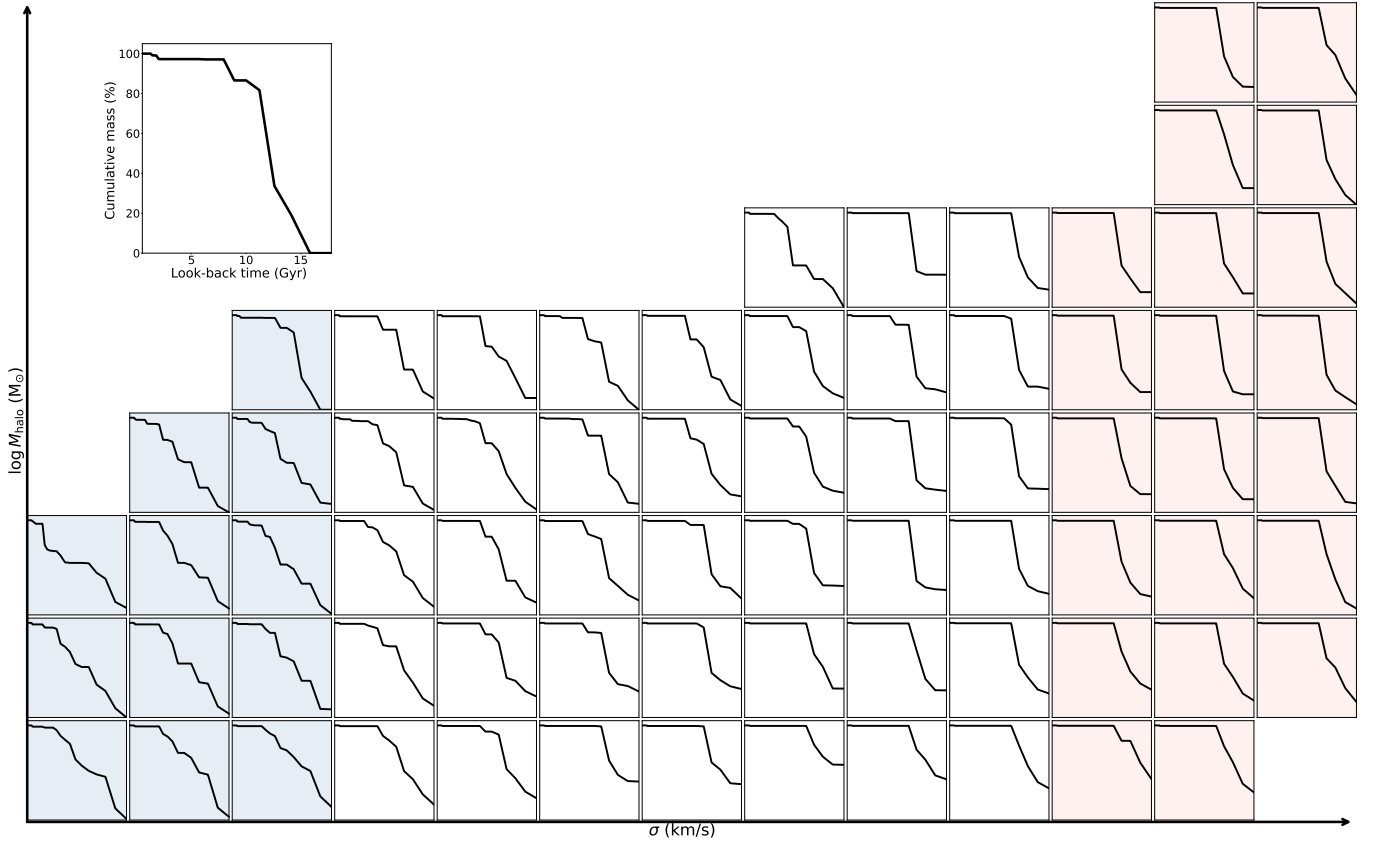


Figure 5. Star formation history for each central galaxy in the full sample, across different ranges of σ (horizontal arrow) and M_{halo} (vertical arrow). Each box represents the cumulative initial mass contribution, attributed to each SSP, as a function of the look-back time (in Gyr). The blue and red shadows highlight the different SFH of low-and-high- σ central galaxies.

gion of the interstellar medium, regardless of the presence of nuclear activity.

Regarding the gas phase of the ISM, variations in the $\text{EWH}\alpha$ can be attributed to different ionising agents such as young main-sequence stars, nuclear activity, and hot evolved low-mass stars (HOLMES). To determine the ionising source in galaxies, we employ comparison techniques utilising the relative fluxes of emission lines. Elliptical galaxies, known for their low emission line intensities, are typically ionised by HOLMES (Binette et al. 1994; Sarzi et al. 2010; Cid Fernandes et al. 2011). We use the ‘‘Baldwin, Phillips & Terlevich’’ (Baldwin et al. 1981, BPT) to identify the ionisation source in our

sample. The BPT diagram, shown in the left panel of Figure 6, indicates that the dominant ionisation pattern of all studied galaxies is LINER. However, while commonly used, Stasińska et al. (2008) show that the LINER region in this diagram contains a combination of two distinct galaxy families: those hosting a weak AGN and those ionised by HOLMES. Therefore, we employ the WHAN diagram (Cid Fernandes et al. 2010) as a supplementary tool. As shown in the right panel of Fig. 6, the WHAN diagram reveals that the typical ionisation source for central galaxies in our sample is HOLMES. Using both diagrams, we show that the emission line ratios and equivalent widths observed in our stacked spectra are fully consistent

with that of “retired” galaxies, objects whose gas ionisation is due to HOLMES. It is important to note that each point in these diagrams represents the stacked data mentioned in Sect. 2.2. Thus, even if individual galaxies within a stack exhibit intense emission lines due to nuclear activity or star formation, the resulting spectrum represents the characteristic ionisation pattern of the overall population within that specific stack. Our analysis confirms that HOLMES remain the primary ionisation source for central galaxies, even when considering ICs and GCs separately (see Figure A2). This is supported by the nearly identical diagnostic diagrams (BPT and WHAN) for these categories.

Our findings indicate that the ionising agent in the central galaxies of our sample is HOLMES, thereby eliminating the possibility of attributing variations in EWH α to a different source. Instead, we interpret these variations in EWH α in relation to σ and M_{halo} as indicators of the mass fraction of ionisable gas within the galaxy. A study by Herpich et al. (2018) supports this interpretation, revealing that elliptical galaxies with EWH α values below 3 Å share the same ionising agent, with differences between retired and passive galaxies primarily reflecting variations in the amount of ionisable gas present in the galaxy.

As far as A_V is concerned its numerical value depends on how the geometry of the grains and the specific efficiency of scattering affects the column density. If this column density is proportional to the column density of the ionised gas, it will also be proportional to EWH α . Consequently, both A_V and EWH α will be indicative of the ISM presence. Their coefficients will be indicators of how much gas there is in the galaxy and also how these quantities vary according to σ and M_{halo} . Therefore, in the subsequent discussion, we will focus only on the results for EWH α , which will indirectly apply to A_V as well.

The observed decrease in EWH α as σ increases (Fig. 3, panels j, k and l) can be attributed to many mechanisms, including mergers, reabsorption of expelled gas by the galaxy itself, or absorption of peripheral gas. While this study does not explore all the possibilities exhaustively, we consider that central galaxies, unlike other ETGs, occupy the central regions of DM halos. As a result, they are more likely to be influenced by gas flows. Therefore, we propose that the differences in H α emission arise from variations in the efficiency of gas accretion and cooling processes, which are influenced by a combination of cooling flows and feedback mechanisms.

The observed increase in EWH α with M_{halo} suggests a potential association with a higher cold gas infall rate. Stott et al. (2012) propose an increased efficiency of the ICM cooling in massive halos to account for differences in the $L_X - T_X$ ratio between low and high M_{halo} systems. In order to provide a quantitative analysis, we develop a theoretical model that examines the interplay between two physical processes: AGN feedback and ICM cooling.

4.3 Modelling the gas emission via ICM cooling flow and AGN feedback

Aiming to understand systematic differences in some properties of BCGs in a sample of 123 X-ray emitting clusters, Stott et al. (2012) investigated the relation between AGN feedback from the BCG and the ICM cooling. The authors argue that the thermodynamics of the ICM is set by the relative importance of the energy E_{AGN} released by AGN feedback over the cluster history to the thermal energy E_{ICM} of the ICM. An estimate of E_{AGN} was obtained for a typical radio-loud galaxy in their sample and expressed as a function of the feedback efficiency η , while considerations involving the dynamical equilibrium and the ICM temperature were then used to estimate

the total thermal energy of the intracluster medium as a function of M_{500}^1 and the ICM temperature T_X as

$$E_{\text{ICM}} = \frac{3k_B}{2\mu m_p} T_X f M_{500}, \quad (2)$$

where f is the ICM mass fraction, k_B the Boltzmann constant, μ is the mean molecular weight of the constituent particles of the ICM and m_p is the proton’s mass.

If the presence of ionisable gas in a central galaxy is due to ICM cooling, the parameterisation of EWH α we have performed in Sect. 3.2 as a function of σ and M_{halo} maps the ICM cooling efficiency as compared to the energy output due to AGN feedback on the ICM. The typical timescales for ICM cooling in the centre of clusters are much lower than 1 Gyr, and so we expect that, for a fixed total thermal energy for the ICM, the occurrence of an emission line in a central galaxy could be therefore the result of the interplay between the energy dissipation of the ICM by X-ray emission and the instantaneous kinetic energy output from AGN feedback, irrespective of the total energy that the latter has released to the ICM over cosmic time. In this case, the ratio ξ between the instantaneous kinetic power of the AGN feedback (PE_{BH}) and the thermal energy of the ICM, (E_{ICM}), i.e.

$$\xi = \frac{PE_{\text{BH}}}{E_{\text{ICM}}}, \quad (3)$$

effectively defines the H α emission in central galaxies. Notice that ξ is equivalent (except for a multiplicative constant) to the $E_{\text{AGN}}/E_{\text{ICM}}$ ratio proposed by Stott et al. (2012) for a fixed AGN lifetime.

In order to model the EWH α observed in our sample of central galaxies, we expand the above prescription, re-writing equation 3 as an explicit function of σ and M_{halo} . We assume that the total mass M_{halo} of the cluster scales as $M_{\text{halo}} \propto M_{500}$ and is also proportional to the cluster total volume, so that $M_{\text{halo}} \propto R^3$, where R is a characteristic radius. We also assume an equilibrium condition where the temperature of the gas, T_X , scales with the average kinetic energy of the galaxies in the cluster, i.e. to the square of the dispersion in the values of the individual velocities of the galaxies of the system (Lubin & Bahcall 1993). For a spherically symmetric, homogeneous and virialised distribution of particles of total mass M and radius R , σ^2 scales with M/R . We then obtain

$$E_{\text{ICM}} \propto \frac{M_{\text{halo}}}{R} M_{\text{halo}} \propto \frac{M_{\text{halo}}}{M_{\text{halo}}^{1/3}} M_{\text{halo}} \propto M_{\text{halo}}^{1.67}. \quad (4)$$

We further assume that the instantaneous kinetic power of the AGN feedback PE_{BH} scales with the accretion rate by the SMBH with a constant efficiency ε , i.e.

$$PE_{\text{BH}} = \varepsilon \dot{M}_{\text{BH}} c^2. \quad (5)$$

We now need a recipe for expressing the accretion rate of the SMBH in terms of the physical parameters that describe the galaxies in each stack, i.e. their σ and M_{halo} . The Bondi (Bondi 1952) mechanism has been shown to be efficient in describing several properties of BCGs (Fujita et al. 2014). In this scenario, the feeding of the SMBH occurs through the accretion of hot gas from its surroundings, when the gravitational potential exceeds the thermal energy of the gas.

¹ The mass contained in a radius within which the density of matter is 500 times the mean mass density of the Universe.

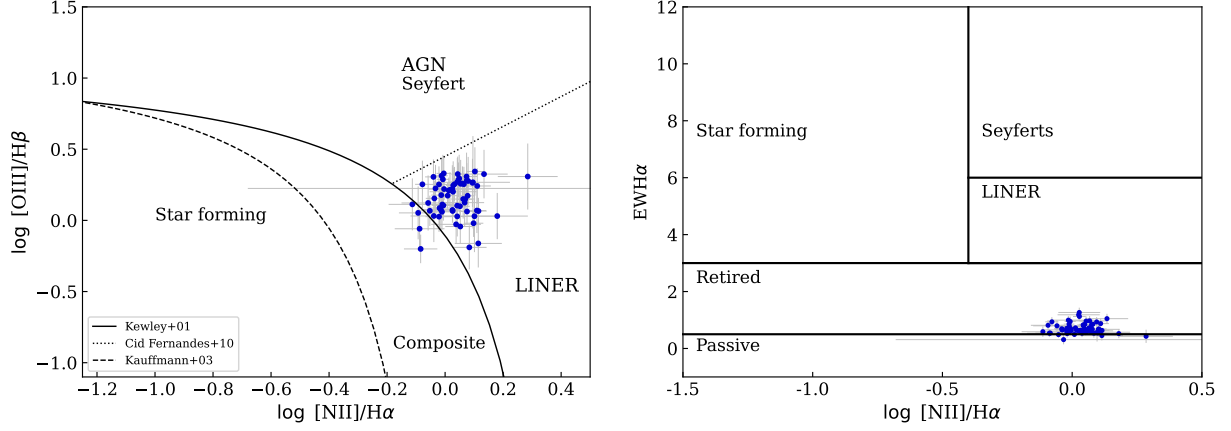


Figure 6. The left panel shows the BPT diagram, which reveals that the dominant ionisation pattern for central galaxies in the full sample is LINER, albeit with some cases exhibiting high uncertainty. In the right panel, the WHAN diagram indicates that HOLMES are the typical ionisation source for the central galaxies in our sample.

This accretion mode is radiatively inefficient, producing a feedback that is mostly mechanical, in the form of jets. The fact that radio galaxies present typically an early-type morphology, and that the probability of an ETG to be a radio galaxy is even higher if it is a central system, reinforces the use of the Bondi scenario as a first approximation. This model implies that the accretion rate of the SMBH is proportional to the square of its mass. Assuming that the gas densities, the speed of sound in the surrounding medium and the Bondi radii are homogeneous across all bins of σ and M_{halo} , we get $\dot{M}_{\text{BH}} \propto M_{\text{BH}}^2$, what results in

$$PE_{\text{BH}} \propto M_{\text{BH}}^2. \quad (6)$$

To explicitly couple PE_{BH} with the global properties of their host galaxies, we use the parameters of the $M_{\text{BH}} - \sigma$ relation derived by Kormendy & Ho (2013). This results in $M_{\text{BH}} \propto \sigma^{4.38}$, and therefore

$$PE_{\text{BH}} \propto \sigma^{8.76}. \quad (7)$$

Substituting the expressions for PE_{BH} and E_{ICM} in equation 3, we finally obtain

$$\xi \propto \sigma^{8.76} M_{\text{halo}}^{-1.67}. \quad (8)$$

Low values of ξ imply that the power of the AGN feedback is small for a fixed total thermal energy of the ICM. This in turn results in large ICM cooling rates; the flow of gas into the central galaxy then enhances $\text{H}\alpha$ emission. The effect of the ICM cooling in the $\text{H}\alpha$ luminosity can therefore be parameterised as

$$L_{\text{H}\alpha} \propto \xi^\gamma, \quad (9)$$

where γ is a *negative* coefficient whose absolute value depends on the detailed physics of ICM cooling and heating mechanisms.

The above prescription for $L_{\text{H}\alpha}$ can be transformed into a similar one for $\text{EWH}\alpha$ in the following way. By definition,

$$\text{EWH}\alpha = \frac{F_{\text{H}\alpha}}{\overline{F_{\text{C}}}}, \quad (10)$$

where $F_{\text{H}\alpha}$ is the flux of the $\text{H}\alpha$ line and $\overline{F_{\text{C}}}$ is the average level of

the spectral continuum at the position of the $\text{H}\alpha$ line. This expression can be converted in a ratio involving $L_{\text{H}\alpha}$ by means of

$$\text{EWH}\alpha = \frac{F_{\text{H}\alpha}}{\overline{F_{\text{C}}}} \frac{4\pi D^2}{4\pi D^2} \equiv \frac{L_{\text{H}\alpha}}{L_{\text{C}}}, \quad (11)$$

where D is the luminosity distance of the galaxy. The factor $L_{\text{C}} \equiv \overline{F_{\text{C}}} 4\pi D^2$ – the average luminosity density of the spectral continuum at the position of the $\text{H}\alpha$ line – can be estimated by the (fibre) luminosity of the galaxy in a spectral window around the $\text{H}\alpha$ line, what roughly corresponds to the high wavelength limit of the passband of the SDSS r filter at the typical redshifts of our sample of centrals. The r -band absolute magnitudes are available from the SDSS, but this is not a good proxy for L_{C} , because in general only a fraction of the galaxy light is included in the SDSS spectroscopic fibre (and this fraction is strongly dependent on the redshift of the galaxy). Assuming that the galaxy is homogeneous and therefore the ratio between the fibre ($f_{r,F}$) and total ($f_{r,T}$) r -band fluxes of the galaxy is equal to the ratio between the respective luminosities ($L_{r,F}$, $L_{r,T}$), we get

$$L_{r,F} = \frac{f_{r,F}}{f_{r,T}} L_{r,T}. \quad (12)$$

Using the CASJOBS² environment, we obtain the values of $f_{r,F}$, $f_{r,T}$ and $L_{r,F}$ for the galaxies in each stack and derive $L_{r,F}$. Finally, we average the $L_{r,F}$ values across all galaxies in a stack to get L_{C} .

It is important to note that L_{C} is the average r -band fibre luminosity per stack; just like other physical parameters, it may also be a function of σ and M_{halo} . We have quantified such dependence in Figure 7, using the same fitting procedure described Sect. 3.2. The best-fit coefficients are obtained using a non-linear method of least squares using the curve fit from SciPy Python library. The uncertainties applied to this method are given by the standard deviation measured for each property for the individual galaxies in each stack. After performing these fits, the $\text{EWH}\alpha$ can finally be expressed as

² <https://skyserver.sdss.org/casjobs/>

$$\log \text{EWH}\alpha \propto [8.76\gamma - (0.75 \pm 0.04)] \log \sigma + [-1.67\gamma - (0.042 \pm 0.006)] \log M_{\text{halo}} \quad (13)$$

for the full sample, and

$$\log \text{EWH}\alpha \propto [8.76\gamma - (0.66 \pm 0.03)] \log \sigma + [-1.67\gamma - (0.153 \pm 0.008)] \log M_{\text{halo}} \quad (14)$$

and

$$\log \text{EWH}\alpha \propto [8.76\gamma - (0.86 \pm 0.04)] \log \sigma + [-1.67\gamma - (0.030 \pm 0.005)] \log M_{\text{halo}}, \quad (15)$$

respectively, for ICs and GCs.

Equations 13 to 15 contain a set of theoretical coefficients of the relation $\text{EWH}\alpha \sim \sigma^A M_{\text{halo}}^B$ that can be directly compared to those obtained in Sect. 3.2. Such coefficients are numerically defined except for the exponent γ , which is an unknown in our model but whose value can be obtained directly by comparison with the measured coefficients in Table 1. It is important to note that, as γ is included in both theoretical coefficients, it can be solved for the value that produces the best agreement between the theoretical and measured ones. We obtain $\gamma_{\text{full}} = -0.05 \pm 0.03$, $\gamma_{\text{iso}} = -0.16 \pm 0.07$ and $\gamma_{\text{group}} = -0.01 \pm 0.01$ for the full sample, ICs and GCs, respectively. Such values result in theoretical coefficients that are consistent with the measured ones (Tab. 1) within 2σ . The existence of a solution for γ that allows for a good match between the theoretical and measured coefficients – and also presents the correct (negative) sign as expected – is suggestive that the AGN feedback power relative to the ICM internal energy indeed regulates the gas flow into the body of the central galaxy.

Isolated centrals are the population for which we obtain the highest absolute value of γ ; taking into account its uncertainty, γ_{iso} is different from zero at more than 95% statistical confidence. This suggests that, for this sub-population, $\text{EWH}\alpha$ responds to the ratio between PE_{BH} and E_{ICM} . The interpretation given earlier to explain the observed trends for the stellar populations for IC still holds: ICs are able to retain their halo of hot gas more efficiently than GCs, which often lose a considerable amount of their gas through environmental processes. By maintaining their halo of hot gas, ICs can continue cooling, forming new stars and replenishing their ionised gas budget, eventually triggering an active phase and repeating this process as long as the gas reservoir exists. This leads to a more extended SFH, a younger and more metal-rich stellar population, and an ionised gas signature regulated by AGN feedback.

On the other hand, the value of γ_{group} is consistent with zero within its uncertainty. If γ is set to zero, then $L_{\text{H}\alpha}$ is independent of the ratio between the kinetic power of the AGN and the thermal energy of the ICM and our model fails to adequately describe the $\text{EWH}\alpha$ values. This suggests that the GCs are less efficient in retaining their hot gas halo compared to ICs and the signal of the interplay between such processes is confounded by other mechanisms that also participate in the heating and cooling of the ICM in GCs. In fact, gas sloshing due to galaxy mergers or simply by the motions of galaxies close to the central regions of the halo – e.g. Ruszkowski & Oh (2011) – may also be relevant sources of ICM heating in the group environment. Conversely, central galaxies in groups are subjected to merging, a phenomenon that can displace the central’s SMBH and effectively disrupt the feeding-feedback cycle (e.g. Chu et al. 2023). The scenario of accretion of gas-rich, low-mass galaxies that we have already invoked to explain the SFH of GCs, may also

play an important role in setting the $\text{H}\alpha$ emission in such galaxies, as it introduces both younger stars and gas. Considering the mass fractions in central galaxies with low σ values shown in Figure 5, it is possible that a significant number of stars have recently been included into the system via mergers; the recently-acquired gas is then ionised by the radiation field of HOLMES, contributing to the $\text{EWH}\alpha$ signature observed in our sample. In short, the gas deposition in central galaxies in groups seems to be more complex than a single AGN power versus ICM thermal energy prescription, as opposed to ICs; instead, other mechanisms that also contribute to ICM heating and cooling processes must play an important role.

5 SUMMARY

In this study, we investigate the stellar population and interstellar medium properties of a sample of 15, 107 early-type central galaxies from the SPIDER survey (La Barbera et al. 2013). The aim is to understand the evolution of the baryonic content in these galaxies. Using optical spectra obtained from SDSS, we derive key parameters including Age, Z , A_V , and $\text{EWH}\alpha$. Our analysis focuses on examining the dependence of these properties on central σ and M_{halo} for both isolated and group centrals. To identify ionisation sources, we employ BPT and WHAN diagnostic diagrams and propose a scenario based on a Bondi accretion regime to describe the gas properties in central galaxies. The summarised findings of our study are as follows:

- We find that ICs and GCs show a similar trend with σ – older and more metal rich stellar populations as σ increases. Additionally, when considering a fixed σ , we observe a trend of younger Ages associated with higher values of M_{halo} s. Remarkably, both ICs and GCs display consistent correlations between these parameters, suggesting a coherent final star formation history. This holds true regardless of whether the central galaxy acquires gas from its own halo (as in ICs) or from accreted gas-rich systems (as in GCs).
- In both ICs and full sample, we observe a consistent increase in A_V and $\text{EWH}\alpha$ as σ decreases and M_{halo} increases. The trends of these parameters with M_{halo} are not clear for CGs due to larger scatter. For ICs, the variation with M_{halo} becomes less evident at $\sigma > 200 \text{ km s}^{-1}$. Also, the variation with sigma flattens out for all systems above 200 km s^{-1} . The similarity between these properties is further supported by the values obtained through our parameterisation, indicating that both σ and M_{halo} serve as indicators of the ionisable gas content in the central galaxies of our sample. The linear combination of these parameters provides valuable insights into the properties of the ionisable gas in these systems.
- In the case of ICs, we successfully reproduce the observed values of $\text{EWH}\alpha$ by utilising a model that takes into account the interplay between the kinetic power of AGN and the thermal energy of the ICM, providing an explanation for gas deposition in these central galaxies. However, when applying the same model to GCs, it fails to adequately describe the $\text{EWH}\alpha$ values. These findings suggest that ICs are more efficient in retaining their hot gas halo compared to GCs. In the case of GCs, the influence of AGN feedback on ICM thermodynamics may be confounded by other mechanisms that also contribute to the heating and cooling processes within the ICM in GCs.

Our findings indicate intrinsic differences between isolated and group central galaxies. Isolated central galaxies effectively retain their hot gas halo, enabling efficient cooling and reheating. In contrast, gas deposition in group central galaxies is a complex process, involving factors beyond the direct interaction between AGN power

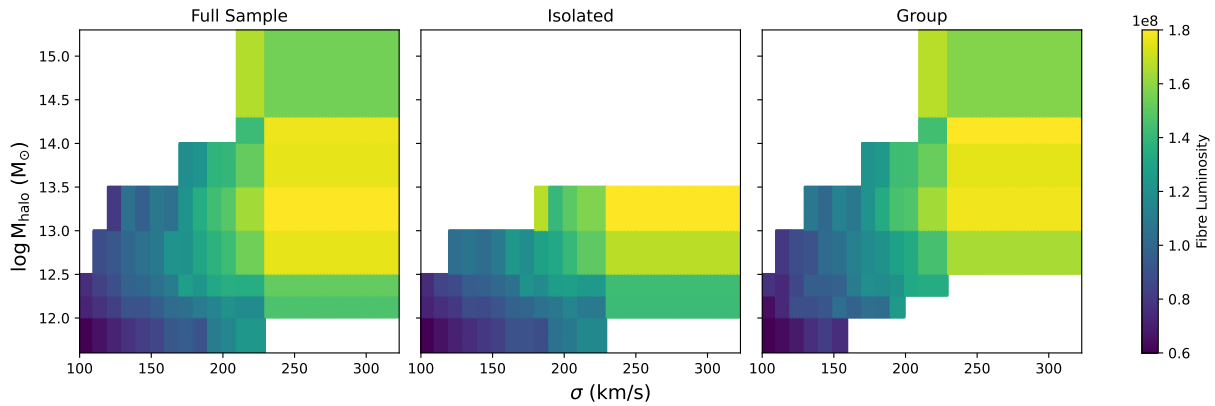


Figure 7. Following the same pattern of Fig. 2, we present the correlation of the fibre luminosity with σ and M_{halo} for each central galaxy bin in the full sample, ICs and GCs, from left to right, respectively.

and the thermal energy of the intra-cluster medium. These observations suggest that the mechanisms governing gas dynamics in isolated and group central galaxies are likely influenced by additional factors.

ACKNOWLEDGEMENTS

VL acknowledges the Coordenação de Aperfeiçoamento de Pessoal de Nível Superior – CAPES scholarship through the grants 88882.427898/2019-01. SBR acknowledges support from Conselho Nacional de Desenvolvimento Científico e Tecnológico – CNPq. RRdC acknowledges the financial support from FAPESP through the grant 2020/15245 – 2.

Funding for SDSS-III has been provided by the Alfred P. Sloan Foundation, the Participating Institutions, the National Science Foundation, and the U.S. Department of Energy Office of Science. The SDSS-III web site is <http://www.sdss3.org/>. SDSS-III is managed by the Astrophysical Research Consortium for the Participating Institutions of the SDSS-III Collaboration including the University of Arizona, the Brazilian Participation Group, Brookhaven National Laboratory, Carnegie Mellon University, University of Florida, the French Participation Group, the German Participation Group, Harvard University, the Instituto de Astrofísica de Canarias, the Michigan State/Notre Dame/JINA Participation Group, Johns Hopkins University, Lawrence Berkeley National Laboratory, Max Planck Institute for Astrophysics, Max Planck Institute for Extraterrestrial Physics, New Mexico State University, New York University, Ohio State University, Pennsylvania State University, University of Portsmouth, Princeton University, the Spanish Participation Group, University of Tokyo, University of Utah, Vanderbilt University, University of Virginia, University of Washington, and Yale University.

This work was made possible thanks to the open-source software packages AstroPy (Astropy Collaboration et al. 2018), Matplotlib (Hunter 2007), NumPy (van der Walt et al. 2011), Pandas (Wes McKinney 2010) and SciPy (Virtanen et al. 2020).

DATA AVAILABILITY

All data used in this article are publicly available at <https://www.sdss3.org/>.

REFERENCES

- Adelman-McCarthy J. K., et al., 2008, *ApJS*, **175**, 297
 Alam S., et al., 2015, *ApJS*, **219**, 12
 Allen S. W., Dunn R. J. H., Fabian A. C., Taylor G. B., Reynolds C. S., 2006, *MNRAS*, **372**, 21
 Astropy Collaboration et al., 2018, *AJ*, **156**, 123
 Baldwin J. A., Phillips M. M., Terlevich R., 1981, *PASP*, **93**, 5
 Best P. N., Kaiser C. R., Heckman T. M., Kauffmann G., 2006, *MNRAS*, **368**, L67
 Binette L., Magris C. G., Stasińska G., Bruzual A. G., 1994, *A&A*, **292**, 13
 Bîrzan L., Rafferty D. A., McNamara B. R., Wise M. W., Nulsen P. E. J., 2004, *ApJ*, **607**, 800
 Bîrzan L., McNamara B. R., Nulsen P. E. J., Carilli C. L., Wise M. W., 2008, *ApJ*, **686**, 859
 Blanton M. R., et al., 2005, *AJ*, **129**, 2562
 Bondi H., 1952, *MNRAS*, **112**, 195
 Bundy K., et al., 2015, *ApJ*, **798**, 7
 Capaccioli M., Caon N., D’Onofrio M., 1992, *Monthly Notices of the Royal Astronomical Society*, **259**, 323
 Cardelli J. A., Clayton G. C., Mathis J. S., 1989, *ApJ*, **345**, 245
 Chandrasekhar S., 1943, *ApJ*, **97**, 255
 Charbonnel C., Meynet G., Maeder A., Schaller G., Schaerer D., 1993, *A&AS*, **101**, 415
 Chu A., Boldrini P., Silk J., 2023, *MNRAS*, **522**, 948
 Cid Fernandes R., Mateus A., Sodré L., Stasińska G., Gomes J. M., 2005, *Monthly Notices of the Royal Astronomical Society*, **358**, 363
 Cid Fernandes R., Stasińska G., Schlickmann M. S., Mateus A., Vale Asari N., Schoenell W., Sodré L., 2010, *Monthly Notices of the Royal Astronomical Society*, **403**, 1036–1053
 Cid Fernandes R., Stasińska G., Mateus A., Vale Asari N., 2011, *MNRAS*, **413**, 1687
 Cid Fernandes R., et al., 2013, *A&A*, **557**, A86
 Croston J. H., Hardcastle M. J., Mingo B., Evans D. A., Dicken D., Morganti R., Tadhunter C. N., 2011, *ApJ*, **734**, L28
 Croton D. J., et al., 2006, *MNRAS*, **365**, 11
 De Lucia G., Springel V., White S. D. M., Croton D., Kauffmann G., 2006, *MNRAS*, **366**, 499
 Dressler A., 1979a, *ApJ*, **231**, 659
 Dressler A., 1979b, *ApJ*, **231**, 659
 Edge A. C., 2001, *MNRAS*, **328**, 762
 Fabian A. C., 1994, *ARA&A*, **32**, 277
 Fujita Y., Kawakatu N., Shlosman I., 2014, arXiv e-prints,
 Gaspari M., Brighenti F., Ruszkowski M., 2013a, *Astronomische Nachrichten*, **334**, 394
 Gaspari M., Ruszkowski M., Oh S. P., 2013b, *MNRAS*, **432**, 3401
 Girardi L., Bressan A., Bertelli G., Chiosi C., 2000, *A&AS*, **141**, 371
 González Delgado R. M., Cerviño M., Martins L. P., Leitherer C., Hauschildt

- P. H., 2005, *MNRAS*, **357**, 945
- González Delgado R. M., et al., 2015, *A&A*, **581**, A103
- Graham A. W., Guzmán R., 2003, *AJ*, **125**, 2936
- Hardcastle M. J., Evans D. A., Croston J. H., 2007, *MNRAS*, **376**, 1849
- Herpich F., Stasińska G., Mateus A., Vale Asari N., Cid Fernandes R., 2018, *MNRAS*, **481**, 1774
- Hlavacek-Larrondo J., et al., 2015, *ApJ*, **805**, 35
- Hunter J. D., 2007, *Computing in Science & Engineering*, 9, 90
- Katayama H., Hayashida K., Takahara F., Fujita Y., 2003, *ApJ*, **585**, 687
- Kormendy J., Ho L. C., 2013, *ARA&A*, **51**, 511
- La Barbera F., de Carvalho R. R., de la Rosa I. G., Lopes P. A. A., Kohl-Moreira J. L., Capelato H. V., 2010, *Monthly Notices of the Royal Astronomical Society*, 408, 1313
- La Barbera F., Ferreras I., Vazdekis A., de la Rosa I. G., de Carvalho R. R., Trevisan M., Falcón-Barroso J., Ricciardelli E., 2013, *MNRAS*, **433**, 3017
- La Barbera F., Pasquali A., Ferreras I., Gallazzi A., de Carvalho R. R., de la Rosa I. G., 2014, *Monthly Notices of the Royal Astronomical Society*, 445, 1977–1996
- Lacerna I., Rodríguez-Puebla A., Avila-Reese V., Hernández-Toledo H. M., 2014, *ApJ*, **788**, 29
- Lequeux J., Peimbert M., Rayo J. F., Serrano A., Torres-Peimbert S., 1979, *A&A*, **80**, 155
- Lintott C., et al., 2011, *MNRAS*, **410**, 166
- Loubser S. I., Sánchez-Blázquez P., Sansom A. E., Soechting I. K., 2009, *Monthly Notices of the Royal Astronomical Society*, 398, 133
- Lubin L. M., Bahcall N. A., 1993, *ApJ*, **415**, L17
- McDonald M., Veilleux S., Rupke D. S. N., Mushotzky R., 2010, *ApJ*, **721**, 1262
- McDonald M., Veilleux S., Rupke D. S. N., Mushotzky R., Reynolds C., 2011, *ApJ*, **734**, 95
- McDonald M., et al., 2012, *Nature*, **488**, 349
- McNamara B. R., Nulsen P. E. J., 2007, *ARA&A*, **45**, 117
- McNamara B. R., O’Connell R. W., 1989, *AJ*, **98**, 2018
- McNamara B. R., Wise M., Sarazin C. L., Jannuzi B. T., Elston R., 1996, *ApJ*, **466**, L9
- McNamara B. R., Rohanizadegan M., Nulsen P. E. J., 2011, *ApJ*, **727**, 39
- O’Dea C. P., et al., 2008, *ApJ*, **681**, 1035
- Oemler A. J., 1976, *ApJ*, **209**, 693
- Oyarzún G. A., et al., 2022, *ApJ*, **933**, 88
- Revaz Y., Combes F., Salomé P., 2008, *A&A*, **477**, L33
- Ruszkowski M., Oh S. P., 2011, *MNRAS*, **414**, 1493
- Salomé P., Combes F., 2004, *A&A*, **415**, L1
- Salomé P., et al., 2006, *A&A*, **454**, 437
- Sarzi M., et al., 2010, *MNRAS*, **402**, 2187
- Schaerer D., Meynet G., Maeder A., Schaller G., 1993a, *A&AS*, **98**, 523
- Schaerer D., Charbonnel C., Meynet G., Maeder A., Schaller G., 1993b, *A&AS*, **102**, 339
- Schaller G., Schaerer D., Meynet G., Maeder A., 1992, *A&AS*, **96**, 269
- Scholz-Díaz L., Martín-Navarro I., Falcón-Barroso J., 2022, *MNRAS*, **511**, 4900
- Somboonpanyakul T., et al., 2022, *AJ*, **163**, 146
- Springel V., Di Matteo T., Hernquist L., 2005, *ApJ*, **620**, L79
- Stasińska G., et al., 2008, *MNRAS*, **391**, L29
- Stott J. P., et al., 2012, *MNRAS*, **422**, 2213
- Vazdekis A., Sánchez-Blázquez P., Falcón-Barroso J., Cenarro A. J., Beasley M. A., Cardiel N., Gorgas J., Peletier R. F., 2010, *MNRAS*, **404**, 1639
- Virtanen P., et al., 2020, *Nature Methods*, **17**, 261
- Voit G. M., Donahue M., 2015, *ApJ*, **799**, L1
- Von Der Linden A., Best P. N., Kauffmann G., White S. D. M., 2007, *MNRAS*, **379**, 867
- Wes McKinney 2010, in Stéfan van der Walt Jarrod Millman eds, Proceedings of the 9th Python in Science Conference. pp 56 – 61, doi:10.25080/Majora-92bf1922-00a
- Yang X., Mo H. J., van den Bosch F. C., Pasquali A., Li C., Barden M., 2007, *ApJ*, **671**, 153
- Yang X., Mo H. J., Zhang Y., van den Bosch F. C., 2011, *ApJ*, **741**, 13
- Zhao D., Aragón-Salamanca A., Conselice C. J., 2015a, *MNRAS*, **448**, 2530
- Zhao D., Aragón-Salamanca A., Conselice C. J., 2015b, *MNRAS*, **453**, 4444
- Zhao D., Aragón-Salamanca A., Conselice C. J., 2015c, *MNRAS*, **453**, 4444
- de Carvalho R. R., Ribeiro A. L. B., Stalder D. H., Rosa R. R., Costa A. P., Moura T. C., 2017, *AJ*, **154**, 96
- van der Walt S., Colbert S. C., Varoquaux G., 2011, *Computing in Science & Engineering*, 13, 22

APPENDIX A:

Tables A1 to A3 present the numbers of central galaxies per σ and M_{halo} bin, along with the S/N (in parentheses) for the full sample, isolated, and group centrals respectively.

In Figure A1, we compare the results from Figure 3 (represented by dashed lines) to the results obtained using GM templates (solid lines). While the parameter values vary as expected, the trends with σ and M_{halo} are very similar.

Figure A2 presents the BPT and WHAN diagnostic diagrams for isolated (blue dots) and group (red dots) centrals. For both the BPT and WHAN diagram, the results for both samples remain consistent with Figure 6.

This paper has been typeset from a $\text{\TeX}/\text{\LaTeX}$ file prepared by the author.

Table A1. Number of Galaxies (Signal-to-noise ratio) per bin of σ and M_{halo} in the full sample.

σ (km s ⁻¹)	log $M_{\text{halo}}/M_{\odot}$							
	11.60 12.00	12.00 12.25	12.25 12.50	12.50 13.00	13.00 13.50	13.50 14.00	14.00 14.30	14.30 15.30
100-110	318 (289)	167 (220)	34 (107)					
110-120	458 (355)	359 (336)	105 (186)	24 (96)				
120-130	506 (392)	499 (396)	168 (245)	40 (127)	5 (74)			
130-140	467 (380)	679 (476)	324 (350)	98 (192)	6 (59)			
140-150	334 (330)	639 (483)	365 (385)	145 (258)	9 (71)			
150-160	248 (305)	617 (497)	520 (459)	243 (319)	21 (101)			
160-170	126 (220)	451 (435)	468 (461)	336 (395)	37 (136)			
170-180	69 (169)	293 (359)	428 (451)	374 (427)	50 (165)	9 (86)		
180-190	45 (142)	212 (311)	344 (421)	445 (474)	83 (219)	6 (77)		
190-200	20 (102)	104 (217)	215 (331)	380 (449)	91 (232)	23 (107)		
200-210	13 (83)	60 (170)	162 (313)	389 (465)	151 (311)	28 (146)		
210-230	14 (98)	42 (149)	114 (267)	448 (538)	306 (460)	78 (241)	6 (82)	6 (93)
230-323		24 (134)	30 (147)	301 (458)	383 (554)	231 (452)	51 (220)	26 (159)

Table A2. Number of Galaxies (Signal-to-noise ratio) per bin of σ and M_{halo} for the isolated centrals.

σ (km s ⁻¹)	log $M_{\text{halo}}/M_{\odot}$							
	11.60 12.00	12.00 12.25	12.25 12.50	12.50 13.00	13.00 13.50	13.50 14.00	14.00 14.30	14.30 15.30
100-110	292 (276)	148 (208)	18 (80)					
110-120	423 (339)	329 (324)	81 (165)					
120-130	458 (373)	454 (379)	128 (211)	14 (80)				
130-140	432 (364)	616 (451)	244 (300)	50 (152)				
140-150	303 (313)	564 (455)	312 (358)	67 (178)				
150-160	221 (289)	569 (475)	425 (415)	128 (228)				
160-170	115 (210)	412 (414)	384 (415)	182 (289)				
170-180	65 (164)	257 (333)	356 (412)	207 (311)				
180-190	41 (135)	183 (288)	283 (381)	269 (376)	5 (73)			
190-200	16 (92)	93 (204)	172 (295)	241 (356)	6 (90)			
200-210	13 (83)	56 (164)	123 (272)	217 (351)	13 (99)			
210-230	14 (98)	39 (142)	91 (238)	250 (393)	33 (157)			
230-323		20 (123)	23 (129)	182 (350)	56 (201)			

Table A3. Number of Galaxies (Signal-to-noise ratio) per bin of σ and M_{halo} for the group centrals.

σ (km s ⁻¹)	log $M_{\text{halo}}/M_{\odot}$							
	11.60 12.00	12.00 12.25	12.25 12.50	12.50 13.00	13.00 13.50	13.50 14.00	14.00 14.30	14.30 15.30
100-110	14 (67)	10 (66)	12 (67)					
110-120	15 (82)	18 (80)	20 (84)	18 (86)				
120-130	16 (81)	24 (95)	33 (118)	26 (105)				
130-140	13 (78)	38 (125)	67 (172)	45 (123)	6 (59)			
140-150	17 (92)	38 (114)	42 (129)	70 (179)	9 (71)			
150-160	16 (81)	31 (121)	71 (171)	109 (222)	20 (98)			
160-170		28 (120)	66 (183)	142 (263)	36 (134)			
170-180		24 (118)	50 (161)	151 (283)	45 (155)	9 (86)		
180-190		15 (92)	44 (160)	160 (282)	74 (208)	6 (77)		
190-200		9 (86)	36 (147)	122 (259)	84 (220)	21 (101)		
200-210			29 (142)	156 (295)	132 (291)	27 (143)		
210-230			19 (117)	175 (353)	262 (425)	73 (235)	6 (82)	6 (93)
230-323				105 (287)	308 (503)	218 (437)	49 (217)	24 (156)

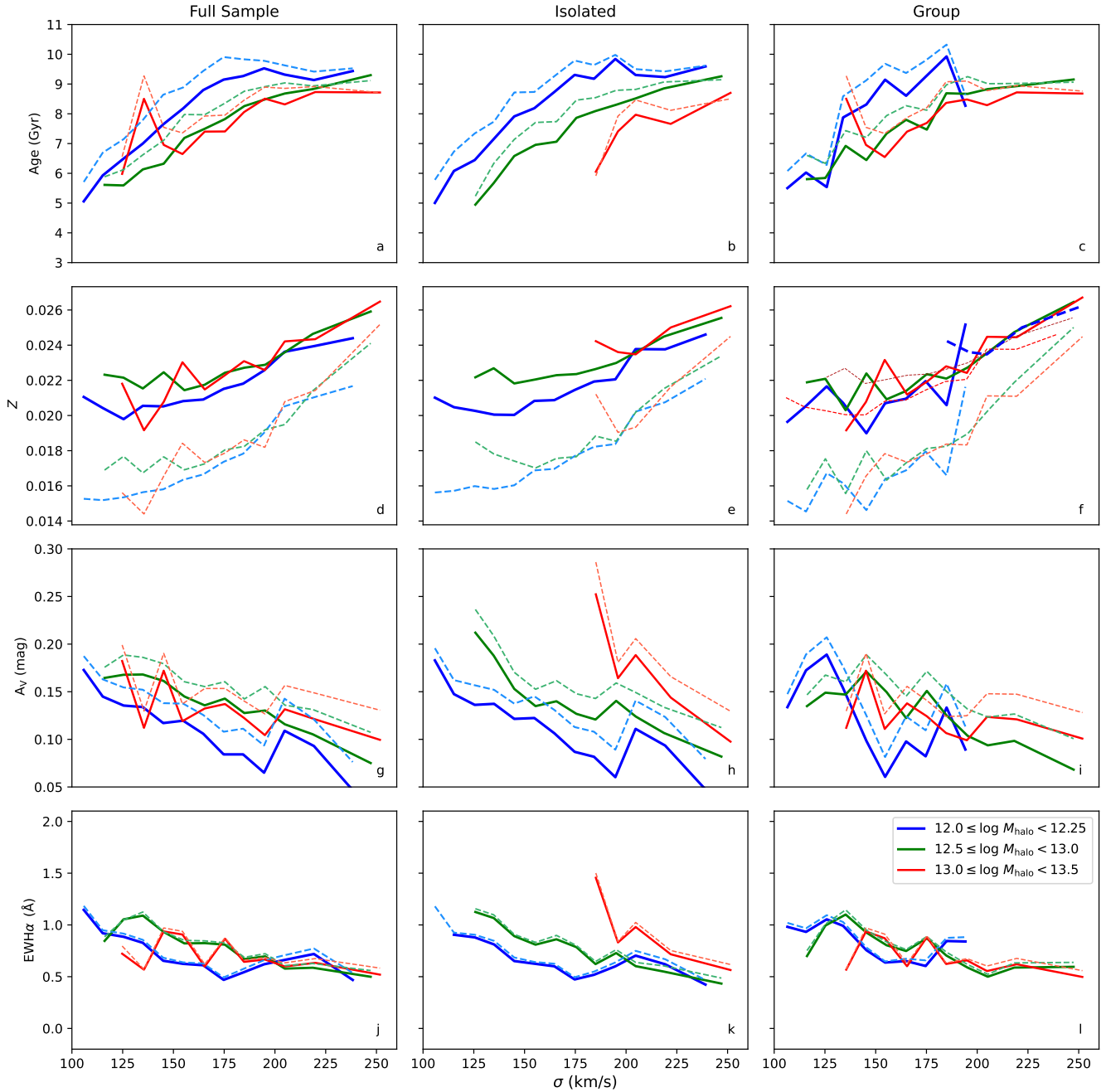


Figure A1. Relationship between Age, Z, A_V , and $\text{EWH}\alpha$ with σ , represented from top to bottom, respectively, for GM templates (solid lines) in comparison to MILES models (dashed lines). The full sample, along with ICs and GCs, is presented from left to right, respectively. Additionally, we included three M_{halo} ranges, distinguished by colours.

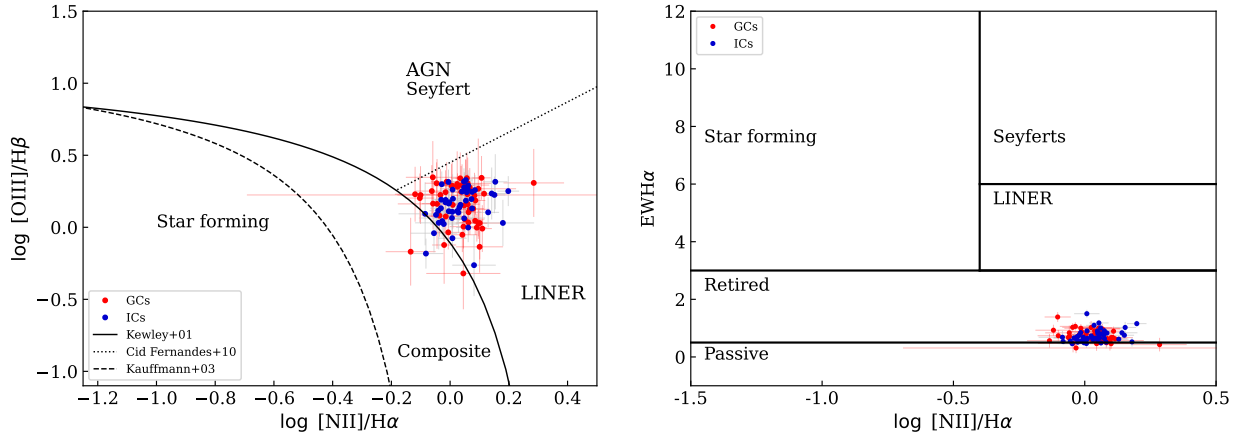


Figure A2. The left panel shows the BPT diagram for ICs (blue dots) and GCs (red dots), which reveals that the dominant ionisation pattern for central galaxies in both sub-samples is LINER, albeit with some cases exhibiting high uncertainty. In the right panel, the WHAN diagram indicates that HOLMES are the typical ionisation source for ICs and GCs.